A Device Model for Rb-Conditioned Chalcopyrite Solar Cells

Tim Kodalle, Hasan A. Yetkin, Alejandra Villanueva Tovar, Tobias Bertram, Reiner Klenk, Rutger Schlatmann, and Christian A. Kaufmann

***Abstract*—We present a comprehensive device model for Cu(In,Ga)Se_2 (CIGSe) thin-film solar cells based on numerical SCAPS-1D simulations. The model reproduces the experimentally determined current-voltage and capacitance-voltage characteristics of a Rb-free reference device, a sample that underwent an RbF-treatment, and a sample based on a CIGSe/Rb$InSe_2$-stack. According to this model, and in agreement with experimental findings, the main consequences of both Rb-conditionings are an increased doping-density and a defect passivation in the CIGSe as well as the formation of a photocurrent barrier at the hetero interface. With the numerical model established, fundamental aspects of the Rb-conditioning, e.g., the differentiation between its effect on bulk and interface recombination are discussed. Additionally, temperature dependent current-voltage analysis is employed in order to test the model's predictions regarding the interaction of Rb with an injection-current barrier at the back contact of the device. Both the simulation and the temperature dependent current-voltage measurements lead to the result that the RbF-PDT is increasing the height of this barrier, while the deposition of Rb$InSe_2$ is decreasing it.**

***Index Terms*—Cu(In,Ga)Se_2 (CIGSe) solar cells, device simulations, RbF-postdeposition treatments (PDT), Rb$InSe_2$, SCAPS.**

I. Introduction

DURING the last 9 years, postdeposition treatments (PDTs) of Cu(In,Ga)Se_2 (CIGSe) thin-films using heavy alkali-fluorides led to several record efficiencies [1]–[4]. Thereby, most studies consistently report the main effects of these PDTs to be an increased carrier concentration of the CIGSe (p_{CIGSe}) [3], [5]–[7], improved minority carrier lifetime (τ_n) [3], [6], therefore, an increased open-circuit voltage (V_{OC}) [2], [3], [5]–[7]. However, the effect of heavy-alkali PDTs on the fill factor (FF) of the devices is reported to be ambivalent. In some studies, a PDT improves FF [2], [6], [8], while in other studies FF is degraded after a PDT [5], [7], [9].

In a recent series of publications, we experimentally investigated the mechanism of an RbF-PDT [5], [10], [11]. Based on these results, we proposed a model explaining both, the beneficial and the detrimental effects of the RbF-PDT. Our core finding is that the beneficial effects of the PDT (on V_{OC} and FF) are due to bulk effects, while detrimental effects (e.g., on the FF) are due to surface/interface effects [9]. We proposed that the Rb passivates deep defects in the bulk of the CIGSe (most likely at grain boundaries) and increases its p-type conductivity via an exchange mechanism with Na. Furthermore, we showed that during the RbF-PDT, a Rb$InSe_2$ (RIS)-layer forms at the surface of the CIGSe [10]. Due to its high bandgap energy (E_{g}) and its high resistivity, we suggested that this layer can, in fact, act as a photocurrent-barrier under forward bias, decreasing FF. Note that this detrimental effect on FF is in competition with the gain in FF one would generally expect to follow a gain in V_{OC} [12]. The thickness and possibly also the coverage of this RIS-layer depend on the Cu-content of the CIGSe, which could, therefore, be the reason for the ambivalent reports regarding the effect of Rb on FF in literature [10].

In the present contribution, we test this model by employing 1-D device simulations using SCAPS-1D [13]. To do so, a device model based on the proposed mechanism has been developed and used to fit the experimentally determined current density-voltage (j-V)- and capacitance-voltage (C-V)-characteristics of the real devices with and without Rb-conditioning.

Please note that this study is the "enhanced manuscript" corresponding to the work we presented recently at the IEEE Photovoltaic Specialist Conference [14]. In addition to the work presented in [14], the present study contains an extended discussion of the role of the RIS-layer and an interface defect proposed by the numerical model. Furthermore, temperature-dependent j-V-measurements are performed in order to further support the main findings of the proposed device model experimentally, i.e., to examine the role of the back contact barrier.

II. Methods

A. Modeling

The device simulations were carried out using SCAPS-1D, version 3.3.07, which was developed at the University of Gent [13].

Manuscript received September 10, 2020; revised October 9, 2020; accepted October 14, 2020. Date of publication November 4, 2020; date of current version December 21, 2020. This work was supported in part by the German Federal Ministry for Economic Affairs and Energy in the frame of the speedCIGS project under Grant 0324095E. *(Corresponding author: Tim Kodalle.)*

Tim Kodalle, Tobias Bertram, Reiner Klenk, and Christian A. Kaufmann Schlatmann are with the Helmholtz-Zentrum Berlin für Materialien und Energie, 12489 Berlin, Germany (e-mail: tim.kodalle@helmholtz-berlin.de; tobias.bertram@helmholtz-berlin.de; tobias.bertram@helmholtz-berlin.de; kaufmann@helmholtz-berlin.de).

Hasan A. Yetkin and Alejandra Villanueva Tovar are with the Technical University Berlin, 10587 Berlin, Germany (e-mail: hasan.yetkin@helmholtz-berlin.de; alejandra.villanueva_tovar@helmholtz-berlin.de).

Rutger Schlatmann is with the Hochschule für Technik und Wirtschaft Berlin, 12459 Berlin, Germany (e-mail: rutger.schlatmann@helmholtz-berlin.de).

Color versions of one or more of the figures in this article are available online at https://ieeexplore.ieee.org.

Digital Object Identifier 10.1109/JPHOTOV.2020.3033426

This work is licensed under a Creative Commons Attribution 4.0 License. For more information, see https://creativecommons.org/licenses/by/4.0/

TABLE I
INPUT PARAMETERS FOR THE SCAPS-SIMULATIONS

Layer Properties				
	CIGSe	CdS	RIS	ZnO
d [μm]	GDOES	0.06	varied	0.15
E_g [eV]	GDOES	2.4	2.8	3.3
E_{EA} [eV]	GDOES	4.3	varied	4.45
n, p [cm^{-3}]	p:varied	n:1·10^{16}	varied	n:1·10^{19}
α [cm^{-1}]	UV-Vis	$\sqrt{h\nu\text{-}E_g}$	UV-Vis	UV-Vis
Neutral (Gaussian) Bulk Defect States				
	CIGSe	CdS	RIS	ZnO
$N_{Def,B}$ [cm^{-3}]	varied	1.8·10^{18}	-	1.8·10^{16}
W_D [eV]	Single	0.1	-	0.1
$E_{Def,B}$ [eV]	VBM+0.5	Mid-gap	-	Mid-gap
σ_e [cm^2]	1.8·10^{-14}	1·10^{-13}	-	1·10^{-12}
σ_h [cm^2]	1·10^{-15}	1·10^{-13}	-	1·10^{-12}
Single Acceptor IF Defect States				
Reference	CdS/CIGSe ('IF')			
RbF-PDT/RIS			CdS/RIS ('IF1')	RIS/CIGSe ('IF2')
$N_{Def,IF}$ [cm^{-2}]	2.3·10^{11}		varied	varied
$E_{Def,IF}$ [eV]	VBM+0.3		VBM+0.3	CBM-0.96
σ_e [cm^2]	1.8·10^{-16}		1.8·10^{-16}	1.8 · 10^{-16}
σ_h [cm^2]	1.2·10^{-14}		1.2·10^{-14}	1.2 · 10^{-14}

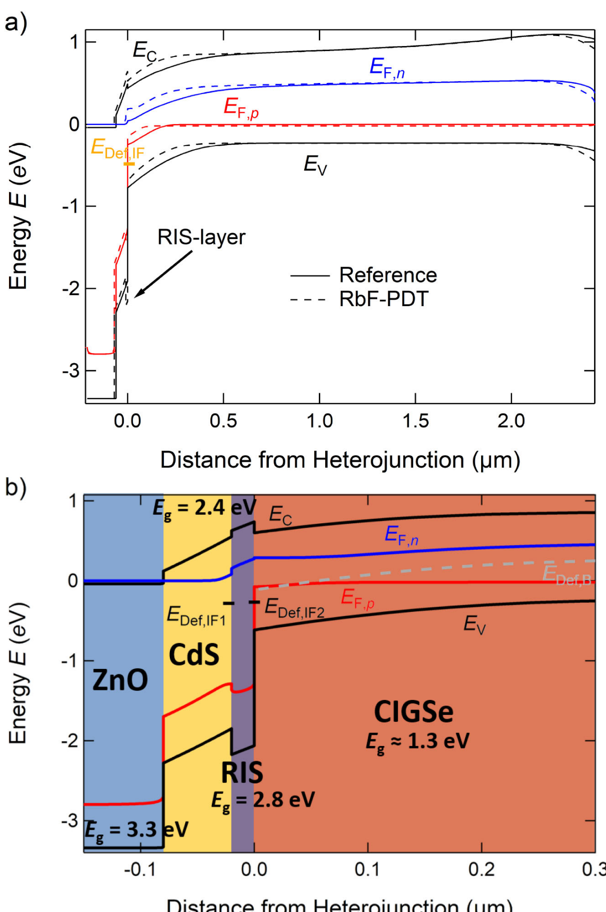

Fig. 1. (a) Simulated energy band diagram of the reference and the RbF-PDT device under illumination without applied bias voltage. For the sake of simplicity, bulk defect levels are not marked. Furthermore, the defect level at the heterointerface is only shown for the Rb-free reference ($E_{\mathrm{Def,IF}}$). (b) Enlarged view of the heterointerface region of a Rb-conditioned device. For the sake of simplicity, the defects in the window layer are not shown. Due to the introduction of the RIS-layer, the former CdS/CIGSe-interface does not exist anymore but instead there are the CdS/RIS- and the RIS/CIGSe-interface with the corresponding defect levels ($E_{\mathrm{Def,IF1}}$ at the former and $E_{\mathrm{Def,IF2}}$ at the latter).

Table I lists the sets of input parameters for the CIGSe, CdS, RIS, and ZnO layers used in this work. Parameters that are not listed were taken from [15]. Note that the energy bandgap E_{g} and the respective energetic position of the bands in the CIGSe-layer were derived from glow discharge optical emission spectrometry (GD-OES) measurements as described in [16]. For all cases, with and without Rb-conditioning, the depth profiles lead to a minimum bandgap energy of (1.09 $\pm$ 0.01) eV (determined by the procedure described in [16]), and an absorber thickness of around 2.4 μm. Together with the properties used for the CdS-layer [15], the bandgap energy at the surface of the absorber layer leads to a spike of about 53 meV at the hetero interface. The absorption coefficient of the CIGSe, the RIS, and the ZnO layers were determined by UV-Vis measurements.

Several defect contributions are implemented. There is a neutral, mid-gap defect in the bulk of each layer representing defect-assisted recombination, while maintaining a simple device model. More complex and realistic defect distributions in the absorber layer have been tested and provided similarly accurate results but lead to computing difficulties. Furthermore, the model contains an acceptor-like defect at the heterointerface. The formation of such an interface defect due to air and light exposure of the absorber layer was discussed in the literature before [17]. Additionally, a back contact barrier was added to the modeled device as proposed in [18]. The reference barrier height, which was estimated using the j-V-curves of some Rb-free baseline devices, was set to Φ_{BC} = 152 meV.

Fig. 1 shows the energy band diagrams of the reference and the RbF-PDT sample. Fig. 1(a) clearly displays the back-contact barriers and in Fig. 1(b) the defect levels of the bulk defects in the CIGSe ($E_{\mathrm{Def,B}}$) and of the interface defects ($E_{\mathrm{Def,IFx}}$) are indicated. The experimental j-V- and C-V-curves of the Rb-free reference device are fitted by varying Φ_{BC}, p_{CIGSe}, and the defect density in the bulk of the CIGSe ($N_{\mathrm{Def,B}}^{\mathrm{CIGSe}}$). Thereby, the latter determines the minority charge carrier lifetime in the bulk. In case of Rb-conditioned devices, we additionally introduced an n-type [10] RIS-layer between CIGSe and CdS [see Fig. 1(b)], and varied its thickness d^{RIS}, its doping density n_{RIS}, and the energetic position of the conduction band of the RIS relative to the CIGSe and the CdS. In SCAPS, this is modeled by varying the electron affinity of the RIS, $E_{\mathrm{EA}}^{\mathrm{RIS}}$ ($\Delta E_{\mathrm{C}} = E_{\mathrm{EA}}^{\mathrm{CdS}} - E_{\mathrm{EA}}^{\mathrm{RIS}}$). The introduction of the RIS leads to the formation of two new interfaces: the CdS/RIS-interface (IF1) and the RIS/CIGSe-interface (IF2). In order to be able to reproduce the measured characteristics, an acceptor-like defect

is positioned at both interfaces (see results). The density of these defects ($N_{\mathrm{Def,IFx}}$) is also a parameter that is varied in the model.

B. Experimental

To test the accuracy of the device model, we prepared solar cells based on three different absorber layers. An Rb-free device ("Reference"), an RbF-treated device ("RbF-PDT"), and an absorber layer onto which we coevaporated a thin RIS-layer ("RIS"). The details of the RbF-PDT [5] and the deposition of the $RbInSe_2$ [11] can be found elsewhere. Apart from these different Rb-conditioning procedures, all samples were prepared using nominally identical deposition processes. In particular, the CIGS-deposition was the same for all three samples. The samples consist of the following layer stacks: soda-lime glass substrate/dc-sputtered Mo/absorber layer/chemical bath deposited CdS-buffer layer/rf-sputtered bi-layer of ZnO and ZnO:Al/Ni-Al-Ni contact grid. The absorber layers were deposited using an adapted three-stage process, as described in [19]. Note that the samples were already used in other studies: the reference and RbF-PDT-sample in [5], and the RIS-sample in [10]. The j-V-measurements were performed under standard test conditions (AM 1.5 spectrum, 1000 W/m^2, 25 °C) using a WACOM A+ dual-source solar simulator, the C-V-measurements were performed using a self-assembled setup based on an Agilent 4284 A LCR meter, and a frequency of $\nu = 100\,\mathrm{kHz}$ for the ac voltage. Total reflectance and total transmission measurements of CIGS and ZnO layers on glass respectively were done in a Lambda 1050 UV-Vis setup by Perkin Elmer. Depth profiling via GD-OES was performed using a GDA650 built by Spectruma GmbH. In order to measure the temperature-dependent j–V-curves, the devices were mounted in an evacuated and liquid N_2-cooled cryostat (CryoVac), contacted, and analyzed using a Keithley 2601 A source measure unit in four-point configuration. The temperature range was varied from 320K to 100K with a step size of 10K. The j-V-curves were measured under illumination with an AM 1.5 solar spectrum and a light intensity of 1000 W m^{-2} using a solar simulator (Oriel VeraSol) equipped with light-emitting diodes.

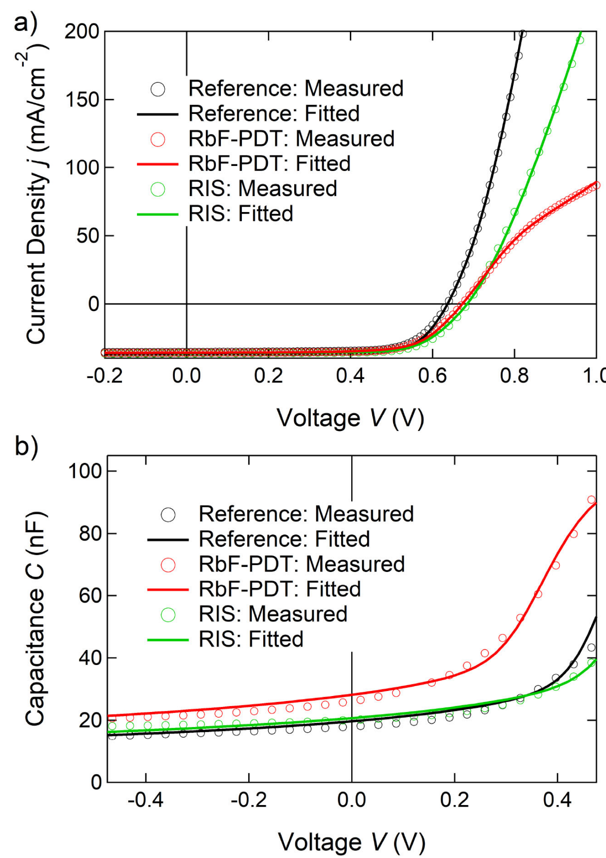

Fig. 2. Results of the corresponding fits in comparison with (a) the experimentally derived j-V- and (b) C-V-curves. Note that the experimental curves were already published before [5], [9].

III. Results and Discussion

A. Evaluation of the Proposed Model

Ideally, a device model provides an accurate fit of the experimentally determined j-V- and also the C-V-curves to ensure that the major defect distributions in the device are accurately chosen. A device model reproducing the j-V- and C-V-curves of the Rb-free reference device can be found rather easily. However, in order to be able to describe the Rb-conditioned devices, several modifications to this reference model have to be implemented. In the following, the main effects of the two different Rb-conditioning procedures, as discussed in the introduction, are listed together with the respective parameter that needed modification in the device simulations.

1) Both the RbF-PDT and the direct RIS-deposition, improve τ_n [3], [6], [19], presumably by the passivation of defects at the grain boundaries [20], [21]. This is represented by a reduction of $N_{\mathrm{Def,B}}^{\mathrm{CIGSe}}$ [dashed gray line in Fig. 1(b)].
2) The RbF-PDT leads to a strong gain in charge carrier concentration p_{CIGSe}[5], the RIS-deposition on the other hand to a lower gain [19]. This is directly implemented into the device model.
3) While the RbF-PDT leads to a strong roll-over in the j-V-curve [5], the RIS-deposition does not [10]. We attribute this behavior to the different deposition temperatures and the subsequently different Na-diffusion mechanisms [19] and, therefore, implemented it into the model by variation of Φ_{BC}.
4) Both the RbF-PDT (at the chosen Cu-content of the CIGSe) and the RIS-deposition, lead to a reduction of FF [10]. This is accounted for by adding the RIS-layer to the device model (see Fig. 1), and adapted to the respective device by varying the parameters d^{RIS}, n_{RIS}, and ΔE_{C}.
5) The RbF-PDT leads to an overall higher capacitance as well as a strong contribution to the capacitance at high forward bias voltages, while both effects are much less pronounced in the RIS-device [see Fig. 2(b)].

The former is accounted for by p_{CIGSe} but the additional contribution to the capacitance at high positive bias voltages has to be represented separately. While there are manifold

explanations for such a strong capacitance gain under forward bias, most of them (e.g., a high defect density of the interface defect at the CdS/CIGSe-IF) lead to the formation of a kink in the simulated j-V-curves (see Section III-B), which is not observed in the experiment [see Fig. 2(a)]. After testing numerous approaches, the additional contribution to the capacitance could only be reproduced in the device simulations (while maintaining a reasonable fit of the j-V-curve) by introducing an additional acceptor like defect at the RIS/CIGSe-IF [see Fig. 1(b)]. By varying its density $N_{\mathrm{Def,IF2}}$, both Rb-conditioned devices can be modeled. Although there is no direct proof for such an interface defect in our measurements, there are hints in the literature [17]. Note that we excluded a possible influence of metastabilities on the C-V-curves by measuring them in both forward and reverse direction—no hysteresis was observed.

Most of the abovementioned parameters are hardly measurable directly. Therefore, the device model can be used to access them by using them as free fit parameters for the experimentally derived j-V- and C-V-curves. Thereby, a combined fitting-procedure in SCAPS was used minimizing the overall deviation of the simulated j-V- and C-V-curves from the experimental ones. The resulting adaptions to the reference model are exemplarily shown for the case of the RbF-PDT-sample in Fig. 1. Fig. 2 shows the experimentally derived j-V- and C-V-curves of all three samples as well as the corresponding SCAPS-fits that were obtained by varying the abovementioned parameters. Table II gives an overview of the results of these fits. The proposed model accurately describes the behavior of the j-V-curves, provides the correct trends of the C-V-curves, and leads to reasonably well-fitting PV-parameters in all three cases (reference, RbF-PDT, and RIS). This overall high agreement of the characteristics derived by the model with the experimentally obtained curves indicates that the model can be used to further understand the mechanism via which the Rb-conditioning is improving the V_{OC} of CIGSe solar cells. To further discuss this, Fig. 3(a) shows the recombination currents for bulk and interface recombination for the reference and Fig. 3(b) for the respective deviation in the cases of the Rb-conditioned devices as extracted from the SCAPS simulations. In all three devices, the recombination current in the bulk ($j_{\mathrm{Rec,Bulk}}$) is at least one order of magnitude higher than the recombination current at the interfaces ($j_{\mathrm{Rec,IF}}$) for all bias voltages, indicating that bulk recombination is the dominant recombination path in the investigated devices. This is in good agreement with the general assumption that the dominant recombination path in highly efficient CIGSe-based solar cells is recombination in the bulk of the absorber layer [22]–[24]. Consequently, the main benefit after RbF-PDT as well as after RIS-deposition—within the presented model—is a reduction of the defect-assisted recombination in the bulk. Furthermore, Table II shows the individual contributions to the Rb-induced V_{OC}-gain for both samples (RbF-PDT and RIS) as extracted from the SCAPS-simulations. Thereby, $\Delta V_{\mathrm{OC}}^{p,\mathrm{CIGSe}}$ is the V_{OC}-gain attributable to the increased carrier concentration in the CIGSe, and $\Delta V_{\mathrm{OC}}^{\mathrm{Bulk}}$ as well as $\Delta V_{\mathrm{OC}}^{\mathrm{IFs}}$ are the V_{OC}-gain due to the reduction of the recombination rate in the bulk and at the interfaces, respectively. These individual contributions were estimated via SCAPS by applying only the respective effect of the Rb-conditioning to the reference model and calculating the corresponding gain in V_{OC} and vice versa. However, since the described mechanisms are all interdependent, no precise values but ranges are given for each contribution. Still, these estimates provide a valuable indication of the impact of the RbF-conditioning on each loss mechanism. Similar to the evaluation of the recombination currents, this estimation shows that the main improvement due to the Rb-conditioning is the passivation of recombination centers in the bulk, which leads to a V_{OC}-gain of one order of magnitude more compared to the interface effects. Additionally, it can be seen that the passivation of bulk recombination is even more effective in case of the RIS-sample compared to the RbF-PDT, which is in good agreement with the fact that a higher elemental concentration of Rb was detected in the bulk of the RIS-sample compared to RbF-PDT samples [10].

TABLE II
RESULTS OF THE FITS OF THE j-V- AND C-V-CURVES

	Reference	RbF-PDT	RIS
τ_n [ns]	48	110	120
p_{CIGSe} [cm^{-3}]	2.9 $\cdot 10^{15}$	5.5 $\cdot 10^{15}$	3.5 $\cdot 10^{15}$
$N_{\mathrm{Def,IF}}$ [cm^{-2}]	2.3 $\cdot 10^{11}$	-	-
$S_{n,\mathrm{IF}}$ [cm/s]	410	-	-
$S_{p,\mathrm{IF}}$ [cm/s]	26000	-	-
$N_{\mathrm{Def,IF1}}$ [cm^{-2}]	-	6.0 $\cdot 10^{10}$	6.0 $\cdot 10^{10}$
$S_{n,\mathrm{IF1}}$ [cm/s]	-	110	110
$S_{p,\mathrm{IF1}}$ [cm/s]	-	7200	7200
$N_{Def,\mathrm{IF2}}$ [cm^{-2}]	-	2.2 $\cdot 10^{11}$	1.0 $\cdot 10^{11}$
$S_{n,\mathrm{IF2}}$ [cm/s]	-	390	180
$S_{p,\mathrm{IF2}}$ [cm/s]	-	26000	12000
Φ_{BC} [meV]	152	272	22
d_{RIS} [nm]	-	9	18
ΔE_{C} [meV]	-	53	61
n_{RIS} [cm^{-3}]	-	$1\cdot 10^{14}$	$1\cdot 10^{14}$
j_{SC} [mA/cm^2]	36.4 (35.5)	36.0 (36.1)	36.1 (36.5)
V_{OC} [mV]	637 (636)	673 (673)	685 (685)
FF [%]	74.7 (72.4)	69.5 (69.5)	71.2 (71.2)
η [%]	17.3 (16.3)	16.9 (16.9)	17.6 (17.8)
$\Delta V_{\mathrm{OC}}^{p,\mathrm{CIGSe}}$ [mV]	-	5 - 8	0 - 2
$\Delta V_{\mathrm{OC}}^{\mathrm{Bulk}}$ [mV]	-	25 - 35	35 - 44
$\Delta V_{\mathrm{OC}}^{\mathrm{IFs}}$ [mV]	-	−3 - 3	3 - 9

In addition to these effects on V_{OC}, the proposed model also accurately reproduces the Rb-induced FF-loss. Thereby, the introduction of the RIS-layer (with its assumed properties) into the device stack is responsible for the reduced FF, as can be seen from Figs. 4 and 5. Fig. 4 shows that both, the alignment of the CBM of the RIS and the neighboring layers as well as the conductivity of the RIS-layer influence FF. Thereby, a cliff-like situation at the CdS/RIS-interface, i.e., a rather high spike at the RIS/CIGSe-interface ($\Delta E_{\mathrm{C}} > 0$), leads to the strongest

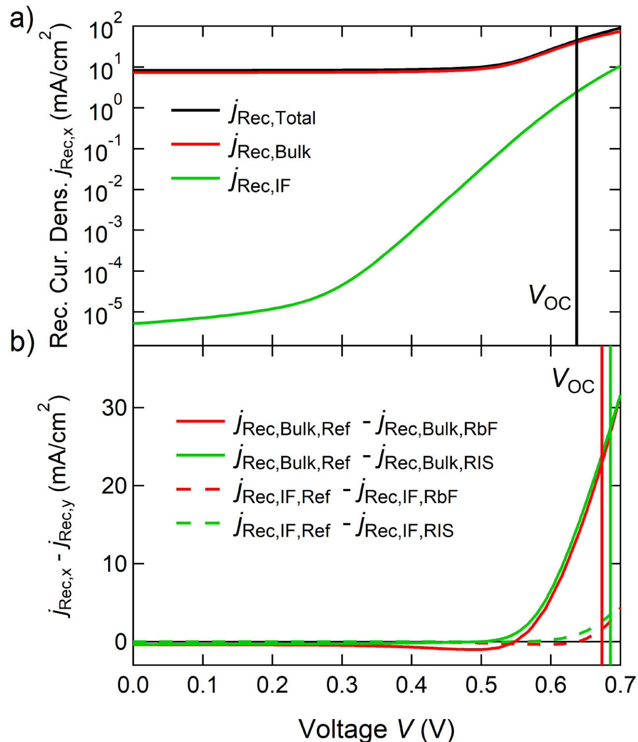

Fig. 3. (a) Recombination currents $j_{\mathrm{Rec},x}$ of the simulated reference device. (b) Difference between the respective recombination currents for bulk- and interface-recombination of the Rb-conditioned devices and the reference device. The straight lines mark the respective V_{OC}.

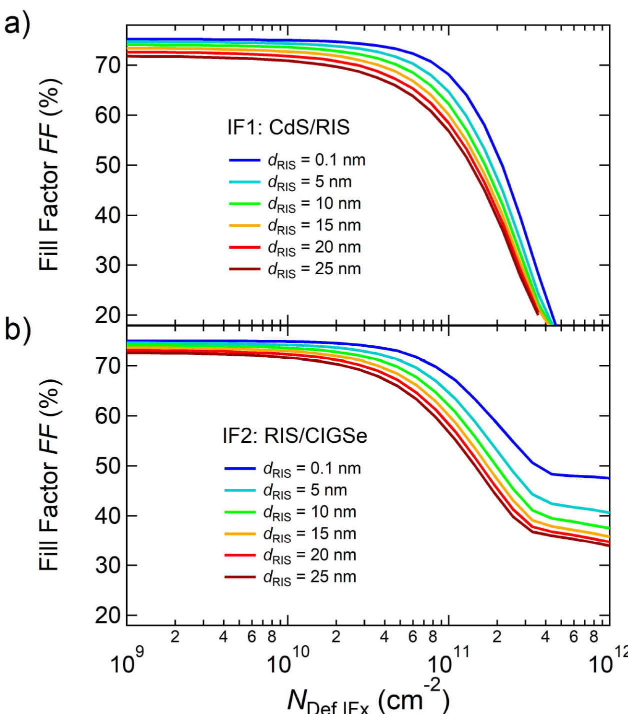

Fig. 5. Simulated trend of the FF in dependence of the defect density of the interface defects. (a) CdS/RIS-interface, "IF1". (b) RIS/CIGS-interface, "IF2," as well as the thickness of the RIS-layer d_{RIS}. If not varied, the following parameters were used for the respective other IF-defect: $N_{\mathrm{Def,IFx}} = 1 \cdot 10^{11}\,\mathrm{cm}^{-2}$. For the RIS-layer, the default parameters given in Fig. 4 were used.

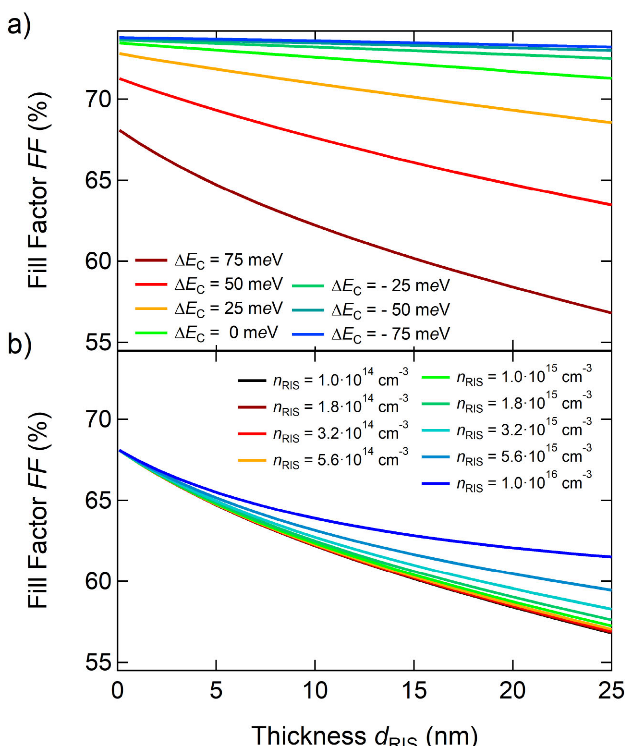

Fig. 4. Simulated trend of the FF in dependence of the thickness of the RIS-layer for two different parameter sets. (a) Variation of the CBM-offset ΔE_{C}. (b) Variation of the carrier concentration n_{RIS}. If not varied, the following parameters were used for the RIS-layer: $\Delta E_{\mathrm{C}} = 75\,\mathrm{meV}, n_{\mathrm{RIS}} = 10^{14}\,\mathrm{cm}^{-3}$.

reduction of FF due to its barrier effect for the photocurrent. Given a certain band line-up, FF is also reduced in case of lower conductivity of the RIS-layer, i.e., low n_{RIS}. Both effects are more pronounced with the thickness of the RIS-layer d_{RIS}. Please note that we generally assume n_{RIS} to be rather low due to the fact that the conductivity of RIS reference thin films is below the detection limit of a standard four-probe measurement.

As can be seen from Fig. 5, the IF-defects can further reduce FF by increasing the barrier at the respective interface due to accumulated charges. Due to this barrier, electrons tend to accumulate in the surface area of the absorber layer under forward bias. This leads to a kink in the j-V-curves if the accumulation of electrons is strong enough to induce a flow of electrons back into the absorber where they recombine leading to a reduced photo current [12]. However, the severity of this effect can be tailored by moderate interface recombination. If some electrons recombine via the interface defect, the accumulation of electrons at the barrier is reduced and the current-flow less influenced [12]. Due to the lower capture probability for electrons from the CIGSe in case of a defect at IF1, the kink is more severe in this case compared to a defect at IF2. However, the defect at IF2 affects the capacitance of the device slightly stronger compared to a defect at IF1 (see Fig. 6), because it is located closer to the Fermi level in the dark [see Fig. 1(b)]. Combining these effects of the IF-defects on j-V- and C-V-curves, it seems more likely that an interface defect at IF2 is present at a significant

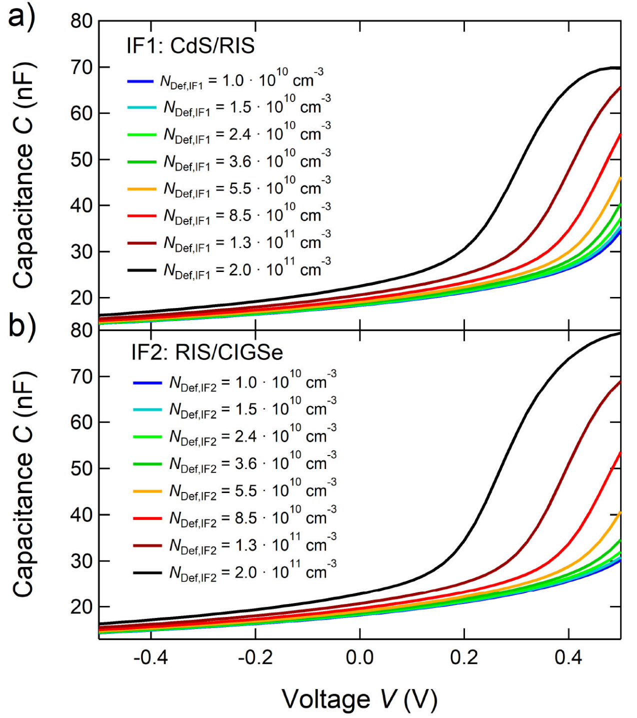

Fig. 6. Simulated influence of the defect density at the interfaces on the C-V-characteristics. (a) Influence of the defect density $N_{\mathrm{Def,IF1}}$, i.e., at the CdS/RIS-interface. (b) Influence of the defect density $N_{\mathrm{Def,IF2}}$, i.e., at the RIS/CIGSe-interface. If not varied, the following parameters were used for the respective other IF-defect: $N_{\mathrm{Def,IFx}} = 1 \cdot 10^{11} \mathrm{cm}^{-2}$. For the RIS-layer, the default parameters given in Fig. 4 were used.

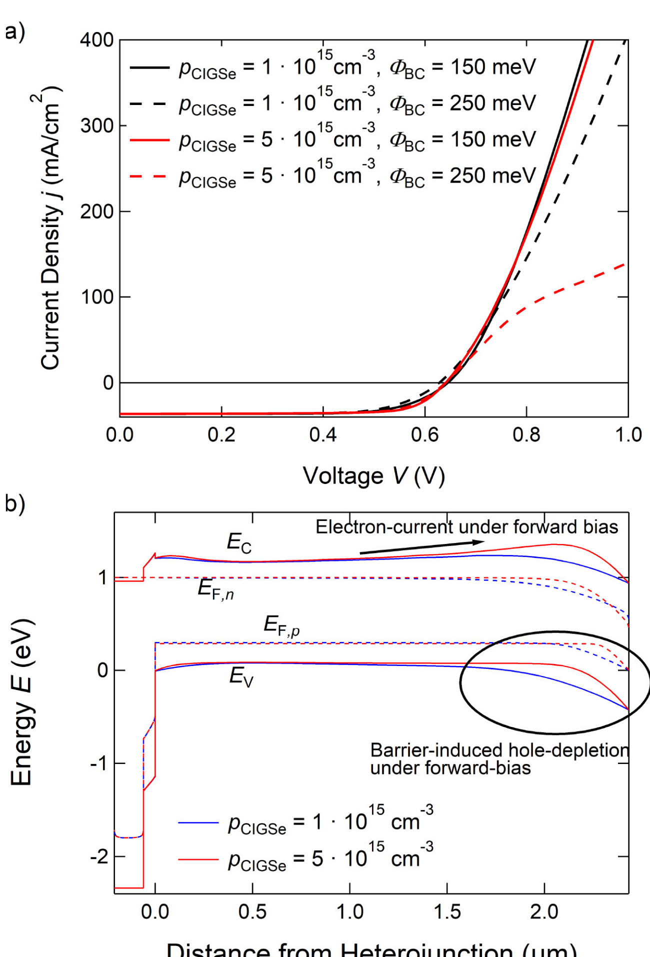

Fig. 7. (a) Influence of the back contact barrier height and the absorber doping on the severity of the roll-over of the j-V-curve. Starting from the reference model, it is shown that only a combination of rather high Φ_{BC} and p_{CIGSe} lead to a strong roll-over at room temperature. (b) Corresponding band-diagrams for the case of $\Phi_{\mathrm{BC}} = 250$ meV. It can be clearly seen how the combination of a Ga-gradient towards the back contact, a high doping density of the absorber layer, and a narrow space charge region at the Schottky interface to the back-contact lead to a barrier for the electron current under injection conditions.

defect density, because no kink is observed in either of the experimental j-V-curves, but a strong capacitance increase is observed in the C-V-curve of the RbF-PDT-sample. Therefore, in the simulations, $N_{\mathrm{Def,IF1}} = 6 \cdot 10^{11} \mathrm{cm}^{-2}$ was fixed, while $N_{\mathrm{Def,IF2}}$ was used as a free fit-parameter (see Table II for fit results). As can be seen from Table II, the RbF-PDT leads to a stronger loss in FF than the RIS-deposition although a thicker RIS-layer forms in the latter case. This is due to the fact that the RIS-deposition also leads to a better passivation of defects at IF2 and in the bulk of the CIGS compensating the FF-loss more effectively than in case of the RbF-PDT. The last feature of the model to be discussed is the roll-over effect observed in the RbF-PDT sample. The severity of the roll over of the j-V-curve is most accurately described by a variation of the barrier height at the back contact Φ_{BC}. While the barrier height of the RbF-PDT sample is about 100 meV higher than in the reference, in the RIS-case, Φ_{BC} is strongly reduced. In addition to the back contact barrier itself, the roll over in the RbF-PDT-case is pronounced by the rather high p_{CIGSe} of this sample. Fig. 7 demonstrates how the manifestation of the roll-over effect interdepends on Φ_{BC} and p_{CIGSe}. If a rather strong barrier is present at the back contact, the adjacent region of the absorber layer is depleted of holes and the current under forward bias is carried by electrons in the CB [25]. Depending on the bandgap-gradient towards the back contact and the doping density of the absorber layer, an additional barrier for these electrons evolves due to the band bending at the Schottky interface, further suppressing the diode current, i.e., pronouncing the roll over of the j-V-curve. In Section III-C, the origin of the back contact barrier and its interaction with the two different Rb-strategies will be further discussed using experimental data.

B. Comparison With Experimental Results and Limitations of the Model

The results of the presented device simulations are generally in good agreement with the experimental results that were observed regarding the mechanism of RbF-PDTs and can help to understand these. This is not only shown by the good agreement of the simulated j-V- and C-V-curves with the experimental curves but also by the fact that all main messages of the model can be supported by experimental data [19]. The main assumption of this model is that the beneficial effects of the Rb-conditioning are almost solely attributable to the

bulk of the absorber layer, while its detrimental effects are attributed to the altered interfaces. In the following, the central elements of the model and the respective (main) influence of the Rb-conditioning are discussed together with the respective experimental results. The density of the deep defect in the bulk representing defect-assisted recombination is reduced by both the RbF-PDT and the RIS-deposition, improving τ_n and V_{OC}. Although the neutral mid-gap defect is merely a representation of the actual defect distributions in CIGSe (see, e.g., [26]), the general effect of Rb, passivating defects in the absorber layer, was shown in several studies, e.g., by time-resolved photoluminescence measurements [3], [6], [19]. The back contact barrier height is increased by the RbF-PDT but decreased by the RIS-deposition, and, therefore, leads to a roll over of the j-V-curve only in case of the RbF-PDT. There are several experimental hints for the presence of such a back contact barrier [10], [18]. However, it is hard to unambiguously identify the reason for an injection-current barrier and it cannot be excluded that there is an additional blocking of the injection-current by Rb-induced modifications of, e.g., the ZnO/CdS-interface as discussed in [27] and [28]. The origin of the back contact barrier and its interaction with both Rb-conditionings is discussed in more detail in Section III-C. The carrier density of the absorber layer is strongly enhanced by the RbF-PDT and less significantly by the direct RIS-deposition. In both cases, this gain has a beneficial influence on V_{OC} but in case of the RbF-PDT, it also enhances the roll-over effect. This is one of the most commonly observed effects in experimental studies, e.g., by capacitance-voltage profiling [3], [5]–[7]. The introduction of the RIS-layer after Rb-conditioning mainly reduces the FF. While the formation of this RIS-layer was experimentally proven by transmission electron microscopy and X-ray photoelectron spectroscopy [5], [29], [30], its role is discussed controversially. In some publications, it was assumed that the formation of a wide-bandgap layer at the CIGS-surface during the RbF-PDT reduces the interface recombination velocity [30]–[32], although no direct evidence was found for this mechanism so far. On the contrary, two studies suspect that this interface layer could—depending on the amount of incorporated Rb—be detrimental for the device performance [9], [10]. The proposed model supports the latter studies, although a beneficial effect of the RIS-layer on the 2-D or 3-D properties of the devices cannot be excluded by the simulations as they are performed here. These might include improved coverage of the surface of the CIGSe by the buffer layer, as suggested in the literature [33], [34]. Note that from the results in literature it is not clear yet whether the RIS-layer completely covers the CIGS or if it grows in islands, similar to the RbF [5]. The introduction of an acceptor defect at the newly formed RIS/CIGSe-interface, which slightly reduces V_{OC}, amplifies the effect of the RIS-layer on FF, and leads to the strong capacitance signal at high bias voltages. This interface defect is a central element of the model because it enables us to describe all major trends in the C-V-curves. Even though an interface defect at the surface of the absorber layer was postulated experimentally [17], its origin and charge state as well as its interaction with the Rb-conditioning have to be further investigated. The fact that its defect density seems to be higher in case of the RbF-PDT, which is done at $T_{\mathrm{Sub}} = 280\,^{\circ}\mathrm{C}$, than in case of the direct RIS-deposition, which is done at $T_{\mathrm{Sub}} = 530\,^{\circ}\mathrm{C}$, (see Table II) might indicate that it is a structural defect, which does not occur at high substrate temperatures or that it is linked to the Na-diffusion, which is different in both cases (see [10]). The proposed model is able to resolve the fundamental discrepancy regarding the effect of the Rb-conditioning on FF in different publications. In agreement with the experimental findings presented in [10], the device model shows that both Rb-conditionings have a beneficial influence on FF (by improving V_{OC} [12], [35]), while on the other hand, the RIS-layer (either formed during the RbF-PDT or directly deposited) decreases FF. The severity of the latter effect and, therefore, the resulting FF are dependent on the exact parameters of the Rb-conditioning and—most importantly—also on the Cu-content of the CIGSe as it was experimentally described in [10]. If one manages to sufficiently suppress the formation of the RIS-layer, the beneficial effect of the Rb-conditioning on FF becomes dominant and an overall FF-gain can be achieved [10]. Since the exact process parameters are different in different laboratories, this can explain the contradictory results published regarding the PDT's effect on FF. Please note that the statement the formation of the RIS-layer should be suppressed' is not contradictory to the fact that the direct RIS-deposition leads to better solar cells than the RbF-PDT. In both cases, a RIS-layer is formed reducing FF but in case of the direct RIS-deposition, the defect passivation in the bulk is more effective (assumingly due to the higher substrate temperature).

C. Temperature-Dependent j-V-Measurements

In order to investigate the roll over of the j-V-curves in more detail, we carried out temperature-dependent j-V-measurements. Fig. 8 shows the resulting $V_{\mathrm{OC}}(T)$-plots for all three samples as well as a linear and a polynomial extrapolation of the measured values to 0K. Although there is a slight reduction of the extrapolated activation energy of the recombination current (E_{a}) after both Rb-conditionings, in all three cases E_{a} is in the range of the minimum bandgap energy as extracted from external quantum efficiency measurements ($E_{\mathrm{g}} \approx 1.10\,e\mathrm{V}$ for reference and RIS and $E_{\mathrm{g}} \approx 1.09\,e\mathrm{V}$ for RbF-PDT), again indicating recombination in the bulk as the dominant recombination path. The result of the polynomial extrapolation of $V_{\mathrm{OC}}(T)$, i.e., the saturation of the measured data and, therefore, the actual $V_{\mathrm{OC}}(0\,\mathrm{K})$, is strongly affected by the Rb-conditioning though. As it was shown in [25] and [36], such a saturation of the $V_{\mathrm{OC}}(T)$ can be attributed to a barrier at the back contact. Although the severity of the saturation (Φ_{jVT}) is proportional to the back-contact barrier height Φ_{BC}, it is not in all cases a reliable quantitative measure for Φ_{BC} due to influences of, e.g., barriers at the hetero interface [36]. Therefore, the experimental results are not used as quantitative measures for Φ_{BC}, but as indicators for a certain trend. And this trend, higher back-contact barrier in the case of RbF-PDT compared to the reference and a lower back contact barrier in the case of RIS, is in very good agreement with the results of the simulations (see Table II). The fact that the RbF-PDT increases, while the RIS-deposition

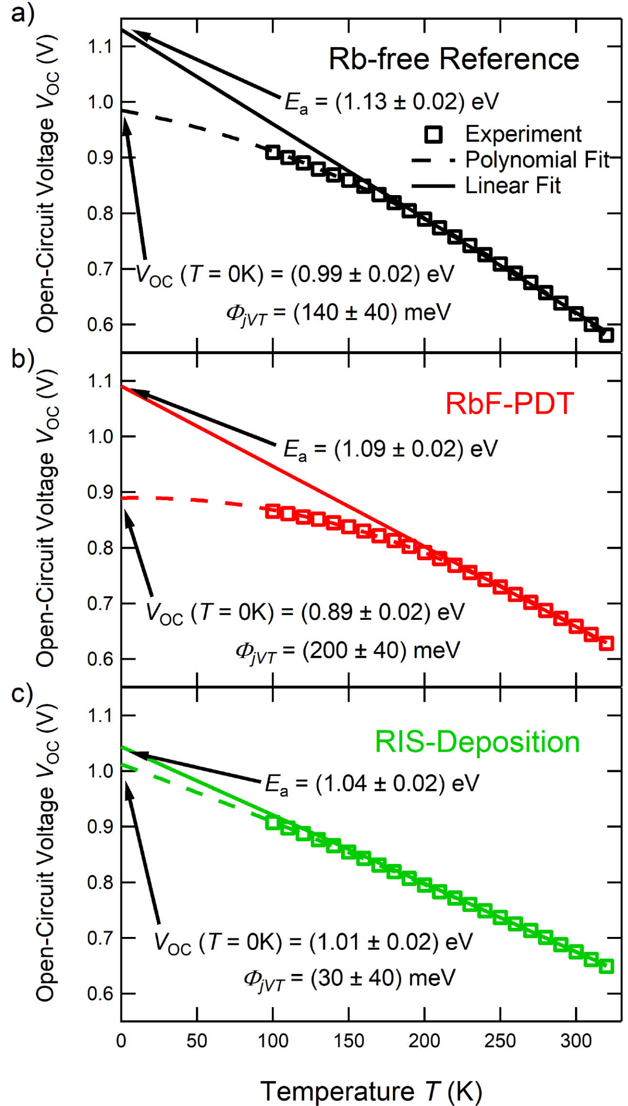

Fig. 8. $V_{\mathrm{OC}}(T)$-results as extracted from temperature-dependent j-V-curves of (a) the Rb-free reference sample, (b) the RbF-PDT-sample, and (c) the RIS-sample. In each subfigure, the measured values are given as open squares, the linear fit as a straight line and the polynomial fit as a dashed line. The back-contact barrier height Φ_{BC} is estimated by the difference of the $V_{\mathrm{OC}}(0\,\mathrm{K})$-values derived from both fits.

decreases Φ_{BC} can be explained by a different Rb-Na-interaction in both cases [5], [10]. As it was shown in [10], the RbF-PDT leads to a strong Na-depletion near the back contact, while the RIS-deposition leads to a slight Na-enrichment in the back contact region. We attributed this behavior to the different substrate temperatures used for both treatments. Due to the rather high temperature during the RIS-deposition (530 °C versus 280 °C during the RbF-PDT), more Na diffuses from the underlying glass into the absorber layer during the RIS-deposition compensating the Rb-Na-exchange mechanism. We speculate that such a Na-enriched absorber/back contact-interface reduces the height of the back contact barrier, e.g., by doping the $MoSe_2$. After the RIS-deposition, the Na-concentration near the back contact was even higher than in the reference, explaining the observed reduction of the barrier height even compared to the reference.

IV. Conclusion

A comprehensive device model is proposed explaining the effects of the incorporation of Rb into CIGSe solar cells. We summarize the widely accepted experimental findings and use them to build a 1-D device model, which is in turn tested by fitting the experimental j-V- and C-V-curves of example devices. The proposed model is able to reproduce and explain these experimentally determined curves, and can furthermore elucidate the effect of both the RbF-PDT as well as the RIS-deposition on the optoelectronic properties of the CIGSe-based devices. Based on the proposed model, we find that the beneficial effects of the Rb-conditioning are almost solely attributable to the bulk of the absorber layer, while its detrimental effects—if present—are attributed to the altered interfaces. While for the bulk, the main effect is the passivation of recombination centers, at the hetero interface it is the formation of a barrier for the extraction current. Furthermore, we show that both the simulations and temperature dependent j-V-curves agree in suggesting that the RbF-PDT leads to a pronounced back contact barrier, while the direct deposition of $RbInSe_2$ at high substrate temperatures reduces the barrier height. Therefore, due to the fact that the RIS-deposition takes only about 4 min, and because of the further improved PV-performance after RIS-deposition, we recommend this procedure as an alternative to the traditional PDT. As shown by the good agreement of the results of the model with the experimental findings, the proposed device model can be further employed to optimize such a RIS-deposition.

Acknowledgment

The authors would like to thank B. Bunn, K. Mayer-Stillrich, J. Lauche, T. Münchenberg, S. Stutzke, and M. Kirsch for preparation of the substrates and finishing of the devices and R. Scheer for fruitful discussions.

References

[1] A. Chirila *et al.*, "Potassium-induced surface modification of Cu(In,Ga)Se_2 thin films for high-efficiency solar cells," *Nat. Mater.*, vol. 12, no. 12, pp. 1107–1111, Nov. 2013.

[2] P. Jackson *et al.*, "Effects of heavy alkali elements in Cu(In,Ga)Se_2 solar cells with efficiencies up to 22.6%," *Physica Status Solidi-RRL*, vol. 10, no. 8, pp. 583–586, Jul. 2016.

[3] T. Kato, J.-L. Wu, Y. Hirai, H. Sugimoto, and V. Bermudez, "Record efficiency for thin-film polycrystalline solar cells up to 22.9% achieved by Cs-Treated Cu(In,Ga)(Se,S)$_2$," *IEEE J. Photovolt.*, vol. 9, no. 1, pp. 325–330, Jan. 2018.

[4] M. Nakamura *et al.*, "Cd-Free Cu(In,Ga)(Se,S)$_2$ thin-film solar cell with record efficiency of 23.35%," *IEEE J. Photovolt.*, vol. 9, no. 6, pp. 1863–1867, Nov. 2019.

[5] T. Kodalle *et al.*, "Elucidating the mechanism of an RbF post deposition treatment in CIGSe thin film solar cells," *Solar RRL*, vol. 2, no. 9, Jul. 2018, Art. no. 1800156.

[6] S. Ishizuka *et al.*, "Group III elemental composition dependence of RbF postdeposition treatment effects on Cu(In,Ga)$_2$ thin films and solar cells," *J. Physical Chemistry C*, vol. 122, no. 7, pp. 3809–3817, Jan. 2018.

[7] S. Karki *et al.*, "Analysis of recombination mechanisms in RbF-treated CIGS solar cells," *IEEE J. Photovoltaics*, vol. 9, no. 1, pp. 313–318, Jan. 2019.

[8] E. Avancini *et al.*, "Effects of rubidium fluoride and potassium fluoride post deposition treatments on Cu(In,Ga)Se_2 thin films and solar cells," *Chemistry Mater.*, vol. 29, no. 22, pp. 9695–9704, Oct. 2017.

[9] T. P. Weiss *et al.*, “Injection current barrier formation for RbF postdeposition-treated Cu(In,Ga)Se_2-based solar cells,” *Adv Mater. Interfaces*, vol. 5, Feb. 2018, Art. no. 1701007.
[10] T. Kodalle, T. Bertram, R. Schlatmann, and C. A. Kaufmann, “Effectiveness of an RbF post deposition treatment of CIGSe solar cells in dependence on the Cu-content of the absorber layer,” *IEEE J. Photovolt.*, vol. 9, no. 6, pp. 1839–1845, Aug. 2019.
[11] T. Kodalle *et al.*, “Properties of co-evaporated $RbInSe_2$ thin films,” *Physica Status Solidi-RRL*, vol. 13, Mar. 2019, Art. no. 1800564.
[12] R. Scheer and H.-W. Schock, *Chalcogenide Photovoltaics: Physics, Technologies, and Thin Film Devices*, vol. 1, Weinheim, Germany: Wiley, 2011, pp. 305–306.
[13] M. Burgelman, P. Nollet, and S. Degrave, “Modelling polycrystalline semiconductor solar cells,” *Thin Solid Films*, vol. 361, pp. 527–532, Feb. 2000.
[14] T. Kodalle, H. A. Yetkin, T. Bertram, R. Schlatmann, and C. A. Kaufmann, “Setting up a device model for Rb-conditioned chalcopyrite solar cells,” in *Proc. 47th IEEE Photovolt. Specialists Conf.*, 2020.
[15] M. Gloeckler, A. L. Fahrenbruch, and J. R. Sites, “Numerical modeling of CIGS and CdTe solar cells: Setting the baseline,” in *Proc 3rd WCPEC*, May 2003, vol. 1, pp. 491–494.
[16] T. Kodalle *et al.*, “Glow discharge optical emission spectrometry for quantitative depth profiling of CIGS thin-films,” *J. Analytical Spectrometry*, vol. 34, no. 6, pp. 1233–1241, Apr. 2019.
[17] T. Hölscher, T. Schneider, M. Maiberg, and R. Scheer, “Impact of air-light exposure on the electrical properties of Cu(In,Ga)Se_2 solar cells,” *Progress Photovolt.*, vol. 26, pp. 934–941, Nov. 2018.
[18] T. Eisenbarth, T. Unold, R. Caballero, C. A. Kaufmann, and H.-W. Schock, “Interpretation of admittance, capacitance-voltage, and current-voltage signatures in thin film solar cells,” *J. Appl. Phys.*, vol. 107, Feb. 2010, Art. no. 034509.
[19] T. Kodalle, “Unraveling the structural and optoelectronic effects of Rb on chalcopyrite solar cells,” Ph.D. dissertation, Martin-Luther-Univ. Halle-Wittenberg, Halle, Germany, Feb. 2020, doi: 10.25673/33525.
[20] P. Schoeppe *et al.*, “Rubidium segregation at random grain boundaries in Cu(In,Ga)Se_2 absorbers,” *Nano Energy*, vol. 42, pp. 307–313, Dec. 2017.
[21] N. Nicoara *et al.*, “Direct evidence for grain boundary passivation in Cu(In,Ga)Se_2 solar cells through alkali-fluoride post-deposition treatments,” *Nat. Commun.*, vol. 10, Sep. 2019, Art. no. 3980.
[22] T. Walter, R. Herberholz, H.-W. Schock, “Distribution of defects in polycrystalline chalcopyrite thin films,” *Solid State Phenomena*, vol. 51–52, pp. 309–316, May 1996.
[23] U. Rau and H.-W. Schock, “Electronic properties of Cu(In,Ga)Se_2 heterojunction solar cells - Recent achievements, current understanding, and future challenges,” *Appl. Phys. A*, vol. 69, pp. 131–147, Aug. 1999.
[24] S. Karki, “Effect of Alkali on the efficiency and reliability of Cu(In,Ga)Se_2 solar cells,” Ph.D. dissertation, Old Dominion Univ., Norfolk, VA, USA, May 2019, doi: 10.25777/q1y5-zw05.
[25] T. Ott *et al.*, “Verification of phototransistor model for Cu(In,Ga)Se_2 solar cells,” *Thin Solid Films*, vol. 582, pp. 392–396, 2015.
[26] G. Hanna, A. Jasenek, U. Rau, and H.-W. Schock, “Influence of the Ga-content on the bulk defect densities of Cu(In,Ga)Se_2,” *Thin Solid Films*, vol. 387, pp. 71–73, May 2001.
[27] A. Villanueva-Tovar, T. Kodalle, C. A. Kaufmann, R. Schlatmann, and R. Klenk, “Limitation of current transport across the heterojunction in Cu(In,Ga)Se_2 solar cells prepared with alkali fluoride postdeposition treatment,” *Solar RRL*, vol. 4, Apr. 2020, Art. no. 190056.
[28] S. Siebentritt *et al.*, “Heavy alkali treatment of Cu(In,Ga)Se_2 solar cells: Surface versus bulk effects,” *Adv. Energy Mater.*, vol. 10, Feb. 2020, Art. no. 1903752.
[29] N. Maticiuc *et al.*, “In vacuo XPS investigation of Cu(In,Ga)Se_2 surface after RbF post-deposition treatment,” *Thin Solid Films*, vol. 665, pp. 143–147, Nov. 2018.
[30] N. Taguchi, S. Tanaka, and S. Ishizuka, “Direct insights into $RbInSe_2$ formation at Cu(In,Ga)Se_2 thin film surface with RbF postdeposition treatment,” *Appl. Phys. Lett.*, vol. 113, Sep. 2018, Art. no. 113903.
[31] T. Lepetit, G. Ouvrard, and N. Barreau, “KF post deposition treatment in co-evaporated Cu(In,Ga)Se_2 thin film solar cells: Beneficial or detrimental effect induced by the absorber characteristics,” *Prog. Photovolt., Res. Appl.*, vol. 25, pp. 1068–1076, Dec. 2017.
[32] E. Handick *et al.*, “Formation of a K-In-Se surface species by NaF/KF post-deposition treatment of Cu(In,Ga)Se_2 thin-film solar cell absorbers,” *ACS Appl. Mater. Interfaces*, vol. 2, pp. 3581–3589, Jan. 2017.
[33] T. M. Friedlmeier *et al.*, “A closer look at initial CdS growth on high-efficiency Cu(In,Ga)Se_2 absorbers using surface-sensitive methods,” in *Proc. 43rd IEEE Photovolt. Specialists Conf.*, Nov. 2016, pp. 457–461, doi: 10.1109/PVSC.2016.7749634.
[34] T. Kodalle *et al.*, “Effects of KF and RbF post deposition treatments on the growth of the CdS buffer layer on CIGS thin films - A comparative study,” *Solar Energy Mater. Solar Cells*, vol. 200, Sep. 2019, Art. no. 109997.
[35] M. A. Green, “Solar cell fill factors: General graph and empirical expressions,” *Solid State Electron.*, vol. 24, no. 8, pp. 788–789, 1981.
[36] T. Ott, T. Walter, and T. Unold, “Phototransistor effects in Cu(In,Ga)Se_2 solar cells,” *Thin Solid Films*, vol. 535, pp. 275–278, 2013.